Viscoelastic full-waveform inversion with spatial probabilistic petrophysical constraints

Odette Aragao & Paul Sava
Center for Wave Phenomena and Dept. of Geophysics, Colorado School of Mines, Golden CO 80401
aquinodearagao@mines.edu

ABSTRACT
Seismic processing and imaging through shallow low-velocity anomalies (e.g., gas clouds) are difficult tasks, as these geological structures can strongly attenuate seismic waves. Thus, estimating accurate attenuation parameters is essential for proper characterization of the subsurface. Full-waveform inversion (FWI) aims to produce high-resolution physical models by iteratively matching modeled with recorded data considering the dynamics and kinematics of waveforms. Even though viscous attenuation plays a major role in seismic wave propagation, attenuation and absorption effects are commonly ignored in most FWI applications, due to the practical challenges of estimating velocity and attenuation simultaneously. A major concern in viscoelastic FWI relates to the strong crosstalk between these parameters due to similar radiation patterns, which creates non-geological artifacts in the inverted models. We propose a strategy to mitigate the interparameter crosstalk and produce geologically feasible models that are consistent with the underlying petrophysics as well as with the seismic data by explicitly imposing petrophysical penalties in the FWI objective function. We consider spatial distribution patterns to classify the available petrophysical data, and build a probability density function (PDF) for each pattern to formulate the penalty term. We illustrate the efficiency of the proposed method with two synthetic examples.

Key words: full-waveform inversion, viscoelastic, attenuation, multiparameter, petrophysics

1 INTRODUCTION

In seismic exploration, FWI aims to build high-resolution subsurface models of complex geological settings, and it relies on wavefield simulation (Tarantola, 1984). Thus, the physics of wave propagation must be as accurate as possible and consistent with the underlying geology. As the Earth is an anelastic medium with viscoelastic properties, the amplitude and phases of the seismic wavefields are affected by absorption that, if not considered during wavefield extrapolation, may hamper the quality of the models delivered by FWI. Shallow low-velocity zones created by gas clouds, for example, lead to strong attenuation, posing substantial challenges for seismic data processing, imaging, and inversion. Therefore, estimating accurate attenuation models, commonly quantified by the quality factor Q, is crucial. Viscoelastic FWI is a promising technique for delivering accurate velocity, as well as attenuation parameters, but joint inversion of these parameters is often ambiguous (Virieux and Operto, 2009). In addition to the intrinsic high non-linearity and ill-posedness nature of multiparameter FWI, the difficulties associated with the severe inter-parameter crosstalk between velocity and attenuation greatly increase the possibility of FWI being trapped in local minima and recovering geologically unfeasible models (Kamei and Pratt, 2013; Operto et al., 2013; Ouellet et al., 2017).

Here, we suggest to reduce the non-linearity and ill-posedness of the viscoelastic FWI problem, as well as to mitigate the artifacts produced by the interparameter crosstalk, by incorporating a penalty term based on petrophysical information into the inversion using a probabilistic approach (Aragao and Sava, 2020a,b). By adapting the framework proposed by Aragao and Sava (2020c), we consider spatial distribution patterns to describe the petrophysical information at every location in the model. We build a PDF for each pattern to formulate a penalty term that is explicitly incorporated in the FWI objection function. To illustrate the

efficiency of the proposed methodology, we use two synthetic examples that contains shallow layers of gas clouds. The petrophysical penalty term based on spatial trends delivers models with high resolution that more accurate than models obtained with unconstrained inversion. Our technique achieve this accuracy by mitigating the crosstalk between velocity and attenuation, as well as by enforcing that the recovered models are consistent with the underlying petrophysics.

2 THEORY

Applications of FWI using attenuation parameters are often formulated in the frequency-domain, because of the implementation simplicity (Malinowski et al., 2011; Kamei and Pratt, 2013; Operto et al., 2015). However, due to heavy computational and memory requirements, frequency-domain cannot handle large-scale simulations (Operto et al., 2007). The time-domain formulation is thus mostly chosen approach when performing viscoacoustic or viscoelastic FWI at several scales (Bai et al., 2014; Plessix et al., 2016; Trinh et al., 2019).

To simulate the viscoelastic wave propagation in the time domain, we describe the elastic anisotropic attenuation by the relaxation function used by Bai and Tsvankin (2016):

$$\Psi_{ijkl}(t) = C^R_{ijkl}(1 + \tau_{ijkl}e^{-t/\tau^\sigma})H(t), \tag{1}$$

where C^R_{ijkl} is the "relaxed stiffness", τ^σ is the stress relaxation time related to the dominant frequency, the parameters τ_{ijkl} describe the difference between the stress and strain relaxation time and quantify the magnitude of anisotropic attenuation. $H(t)$ is the Heaviside function and t denotes time. Equation 1 encompasses only one relaxation mechanism, which can adequately describe quality factors Q when proper parameters are used (Zhu et al., 2013). For $t = 0$, $\Psi_{ijkl} = C^U_{ijkl}$, which corresponds to the "unrelaxed stiffness", such that $C^U_{ijkl} = C^R_{ijkl}(1+\tau_{ijkl})$. Since ΔC_{ijkl}, the difference between the unrelaxed and relaxed stiffness, is proportional to τ_{ijkl}, it reflects on the magnitude of attenuation.

We use Thomsen-style parameters to describe the P- and SV-wave attenuation in VTI media: $A_{P0} \approx 1/(2Q_{33})$ and $A_{S0} \approx 1/(2Q_{55})$ are the P- and SV-wave attenuation coefficients, respectively; ϵ_Q corresponds to the fractional difference between the horizontal and vertical P-wave attenuation coefficients; and δ_Q is related to the curvature of the P-wave attenuation coefficient at the symmetry axis. One can combine these anisotropic attenuation parameters to C^U_{ijkl} in order to compute ΔC_{ijkl} and then estimate quality factor elements Q_{ijkl}. Here, we use the notation Q_{P0} and Q_{S0} instead of Q_{33} and Q_{55}, respectively.

The viscoelastic stress-strain relationship is given by

$$\sigma_{ij} = C^U_{ijkl}\,\epsilon_{kl} + \Delta C_{ijkl}\,r_{kl}, \tag{2}$$

where σ_{ij} and ϵ_{kl} are the stress and strain tensor, respectively, and r_{kl} are the memory variables (Bai and Tsvankin, 2016).

For the purpose of this work, we solve the FWI problem in order to recover v_{P0} and A_{P0} (or Q_{P0}). We set the other velocity (v_{S0}, ϵ and δ) and attenuation parameters (A_{S0}, ϵ_Q and δ_Q) to their true values during the inversion. We minimize an objective function $\mathcal{J}$ composed of the data misfit term $\mathcal{J}_D$ and a petrophysical term that penalizes the models using petrophysical information $\mathcal{J}_P$

$$\mathcal{J}(\mathbf{u}, V_{P0}, A_{P0}) = \mathcal{J}_D(\mathbf{u}, V_{P0}, A_{P0}) + a\,\mathcal{J}_P(V_{P0}, A_{P0}), \tag{3}$$

where $\mathbf{u}(e, \mathbf{x}, t)$ is the viscoelastic wavefield, e and $\mathbf{x}$ are, respectively, the experiment index and space coordinates; and the scalar parameter a determines the relative strength of $\mathcal{J}_P$ in the objective function. The data misfit term $\mathcal{J}_D$ is based on the l_2-norm of the residuals $\mathbf{r}_D(e, \mathbf{x}, t)$ between the modeled data and the observed data, such that

$$\mathbf{r}_D(e, \mathbf{x}, t) = \mathbf{W}_u(e, \mathbf{x}, t)\mathbf{u}_s(e, \mathbf{x}, t) - \mathbf{d}_{obs}(e, \mathbf{x}, t), \tag{4}$$

where $\mathbf{W}_u(e, \mathbf{x}, t)$ are weights that restrict the source wavefield $\mathbf{u}_s(e, \mathbf{x}, t)$ to the known receiver locations, and $\mathbf{d}_{obs}(e, \mathbf{x}, t)$ are the observed data. We compute the gradient of $\mathcal{J}_D$ in respect to the model parameters using the adjoint-state method (Plessix, 2006; Bai et al., 2017).

Aragao and Sava (2020a) propose a petrophysical penalty $\mathcal{J}_P$ calculated using a single PDF derived from all available petrophysical data. The components of the model parameters are represented by the vector $\mathbf{m}(\mathbf{x})$, while the PDF is determined in the petrophysical space of coordinates $\mathbf{p}$. Subsequently, Aragao and Sava (2020b) use multiple PDFs obtained by clustering petrophysical information through K-means when calculating the penalty term, such that each PDF represents a lithological unit. However,

the technique presented by Aragao and Sava (2020b) does not consider spatial trends in the petrophysical data, which may vary laterally and with depth due to depositional and burial regimes (Mavko et al., 2003).

Here, we modify the idea proposed by Aragao and Sava (2020c), to use a petrophysical penalty term based on multiple PDFs that considers spatial distribution patterns of subsurface formations. In order to construct the multiple spatially-variable PDFs, we interpret the petrophysical data and classify different lithologies or formations according to their spatial location.

As the viscoelastic model parameters v_{P0} and A_{P0} have different magnitude and units, we define $\mathbf{m}(\mathbf{x}) = \{c_1\, v_{P0}(\mathbf{x}), c_2\, A_{P0}(\mathbf{x})\}$ and $\mathbf{p} = \{c_1\, v_{P0_p}, c_2\, A_{P0_p}\}$, using coefficients c_1 and c_2 with units and magnitude inverse to v_{P0} and A_{P0}, respectively. Assuming n PDFs defined at different positions in the model, we consider $f_i(\mathbf{p})$ as the probability density of the i-*th* PDF, $i = 1 \ldots n$. Therefore, we can define the distance $D_i(\mathbf{m})$ from the model parameter $\mathbf{m}(\mathbf{x})$ to the i-*th* distribution as

$$\frac{1}{D_i(\mathbf{m})} = \sum_{\mathbf{p}} \frac{f_i(\mathbf{p})}{d_i(\mathbf{m}, \mathbf{p})}, \tag{5}$$

where $d_i(\mathbf{m}, \mathbf{p})$ corresponds to the distance from any given model represented by coordinates $\mathbf{m}$ to any point in the petrophysical space. We formulate the new petrophysical penalty term $\mathcal{J}_P$ as

$$\mathcal{J}_P = \sum_{i=1}^{n} \sum_{\mathbf{m}} K_i(\mathbf{m}) D_i(\mathbf{m}), \tag{6}$$

such that $K_i(\mathbf{m})$ are non-overlapping masks, which depend on $\mathbf{m}(\mathbf{x})$. The role of K_i is to associate each point in the model to its correspondent PDF $f_i(\mathbf{p})$.

3 EXAMPLES

We illustrate our viscoelastic FWI method with two synthetic examples and compare inversions with and without the petrophysical term of the objective function.

For the first example, we use a simple structure with rectangular low-velocity anomalies and a deep horizontal reflector. The low velocity anomalies simulate gas clouds, and the presence of these shallow anomalies can cause strong lateral and vertical variations in seismic wave velocities, as well as significant scattering and amplitude loss due to absorption. We aim to verify if the viscoelastic FWI is successful in imaging the deep reflector as well as the low velocity anomalies when well-log information based on spatial trends in the petrophysical data is incorporated into the inversion.

In the second example, we use a complex model with a more realistic geological setting featuring shallow gas and localized slow velocity anomalies. We demonstrate that petrophysical penalties based on spatially-variable PDFs deliver accurate model updates and mitigate the strong interparameter crosstalk artifacts between velocity and attenuation parameter that severely hamper the models recovered using only the data misfit.

3.1 Model 1: Rectangular low-velocity anomalies

The first synthetic example (Figure 1) uses a model with two rectangular low-velocity anomalies centered at $x = 1.0$ km, with 0.6 km width and 0.03 km thickness, and a flat reflector at $z = 1.25$ km. We use 41 sources at $z = 0.02$ km and a line of multicomponent geophones at $z = 0.05$ km in order to simulate the multicomponent data. We initiate the inversion with models of constant $v_{P0} = 2.0$ km/s and $A_{P0} = 0.005$ (i.e., $Q_{P0} = 100$), which correspond to the background of the true models (Figure 1). We keep the velocity parameters v_{S0}, ϵ and δ equal to their true values during the inversion: $\epsilon = 0.25$ and $\delta = 0.05$, and $v_{S0} = 1.0$ km/s and $v_{S0} = 1.5$ km/s above and below the reflector (Figure 1), respectively. We also keep the attenuation parameter A_{S0} equal to its true values during the inversion: $Q_{S0} = 75$ and $Q_{S0} = 100$ above and below the reflector, respectively. We set ϵ_Q and δ_Q equal to -0.1 and -0.2, respectively.

We consider that prior petrophysical data, corresponding to v_{P0}, from a well located at $x = 1.0$ km are available (Figure 2a). We simulate the well log by adding random noise to the true model (Figure 1) at $x = 1.0$ km. Many methods have been proposed in order to estimate P- and S-wave attenuation logs from available well log data (Cheng et al., 1982; Neep, 1995; Sun et al., 2000), since Q_{P0} values correlate well with petrophysical properties, and thus we assume that an empirical A_{P0} well log derived from a given method is available. For this example, we set $c_1 = 1\, s/km$ and $c_2 = 100$. Figure 2b shows the considered well log for $c_2\, A_{P0} = 50/Q_{P0}$.

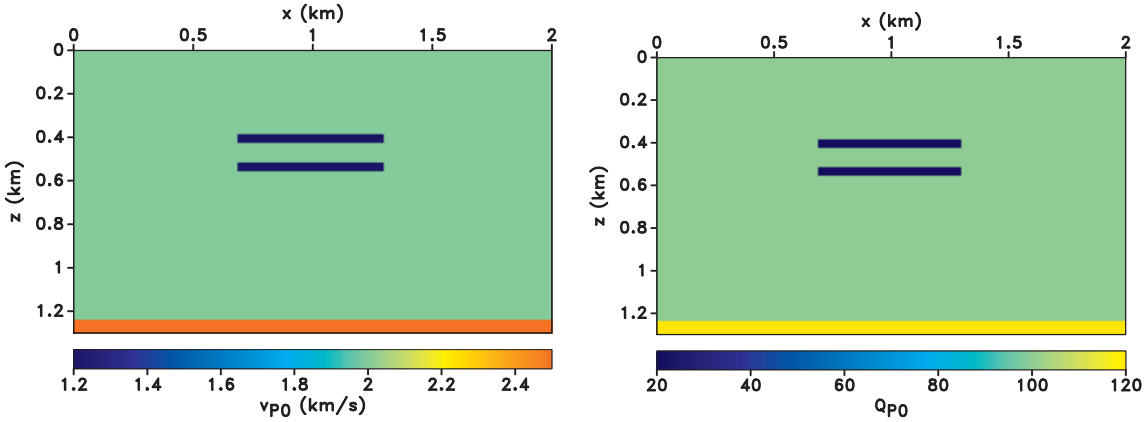

(a) (b)

Figure 1. Synthetic models for the (a)v_{P0} and (b)Q_{P0} models.

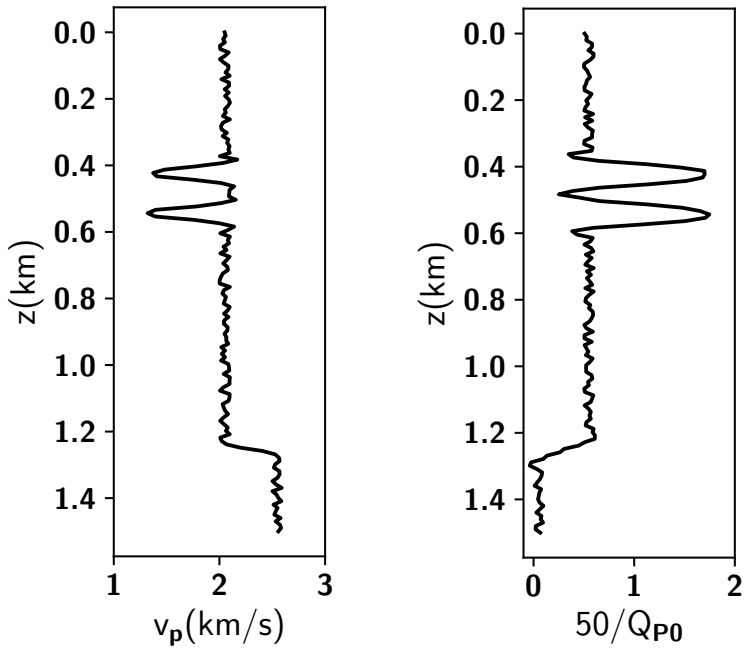

(a) (b)

Figure 2. Hypothetical (a) v_P and (b) Q_{P0} logs at $x = 1.0$ km. We add random noise to the true vertical section in order to calculate v_P and assume that Q_{P0} is determined using an empirical relationship between seismic attenuation and petrophysical properties.

The well logs in Figure 2 indicate the occurrence of four intervals with different velocity and attenuation properties. Therefore, we define the probability distributions $f_i(\mathbf{p})$ and the mask operators K_i, $i = 1 \dots 4$. Therefore, $f_1(\mathbf{p})$ and $f_4(\mathbf{p})$ use the well log above $z = 0.36$ km and below $z = 1.22$ km, respectively; $f_2(\mathbf{p})$ uses the well log between $z = 0.36$ km and $z = 0.56$ km, and $f_3(\mathbf{p})$ uses the well log between $z = 0.56$ km and $z = 1.22$ km. Figures 3a-d show the distributions $f_i(\mathbf{p})$, $i = 1 \dots 4$, respectively. The four masks shown in Figure 4 indicate in which region each PDF $f_i(\mathbf{p})$ is defined. Figures 5a-d display the distances $D(\mathbf{m})$ and the gradient of the petrophysical terms for $f_i(\mathbf{p})$, $i = 1 \dots 4$, respectively. One can notice that, when the model $\mathbf{m}$ at a given location in the updated model is consistent with the distribution given by its correspondent PDF, the distance $D(\mathbf{m})$ and the associated objective function-gradient are both zero. In this case, the data misfit $\mathcal{J}_D$ fully controls the inversion gradient for the model at that location. Otherwise, the corresponding penalty forces the model to comply with the underlying petrophysical PDF.

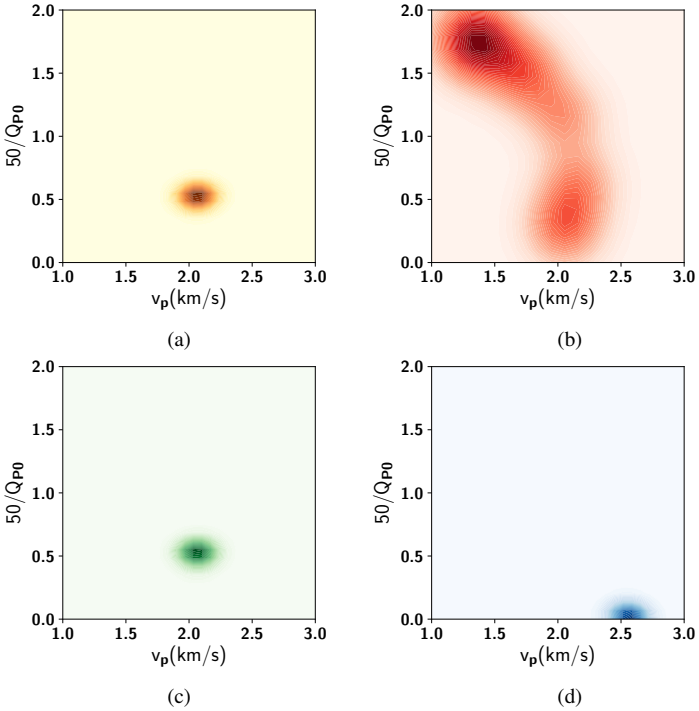

Figure 3. The distributions (a) f_1, (b) f_2, (c) f_3, and (d) f_4 using the spatial trends in petrophysical information from the well log in Figure 2.

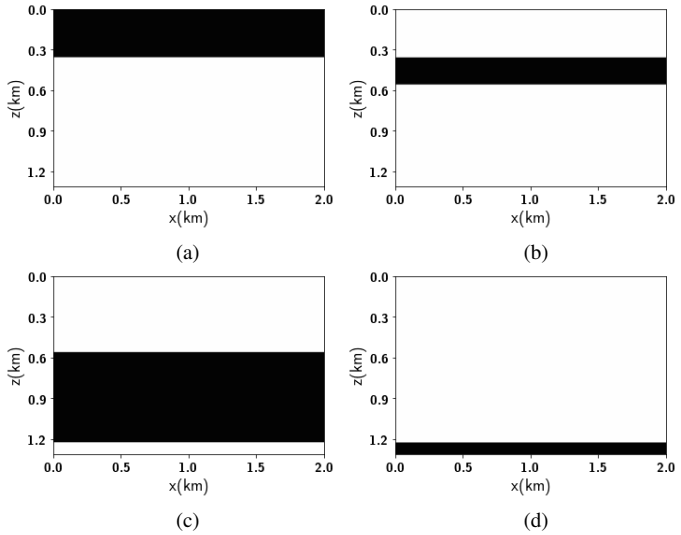

Figure 4. Mask operators used to constrain PDFs at various corresponding spatial locations. Panels (a)-(d) correspond to K_1-K_4. Black regions corresponds to 1, and white to 0.

Figure 6 shows the recovered v_{P0} and Q_{P0} models using the objective function $\mathcal{J}_D$. Without imposing any petrophysical penalties, the reflector at $z = 1.25$ km (Figure 1) cannot be identified in both models, as the reflector is likely masked by the multiples that are created by the gas clouds. In addition, the gas clouds are not recovered during the inversion. Also, the Q_{P0} model is strongly hampered by non-geological artifacts due to the severe trade-off between the attenuation and velocity parameters.

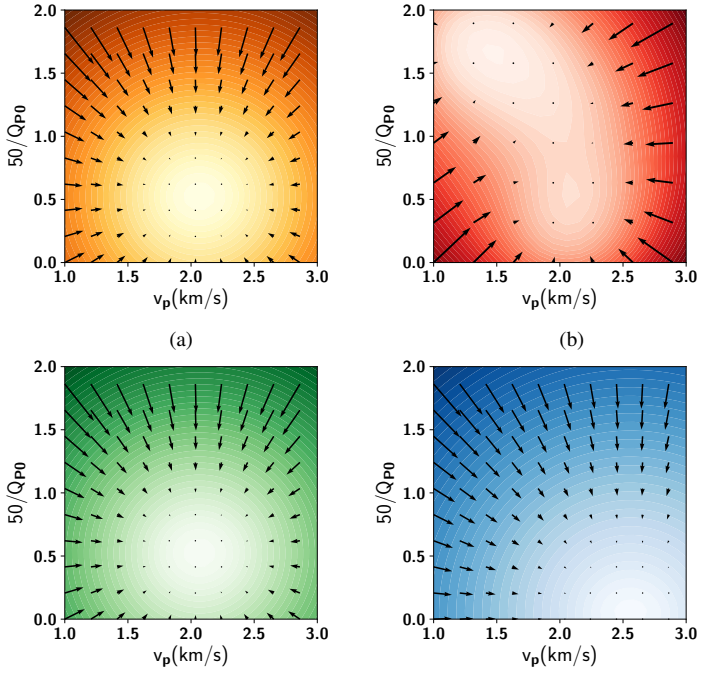

Figure 5. The distance $D_i(\mathbf{m})$ and its gradient for the distributions (a) f_1, (b) f_2, (c) f_3, and (d) f_4 (Figure 3). Note that high probability models are associated with small values of $D_i(\mathbf{m})$ and with zero gradients.

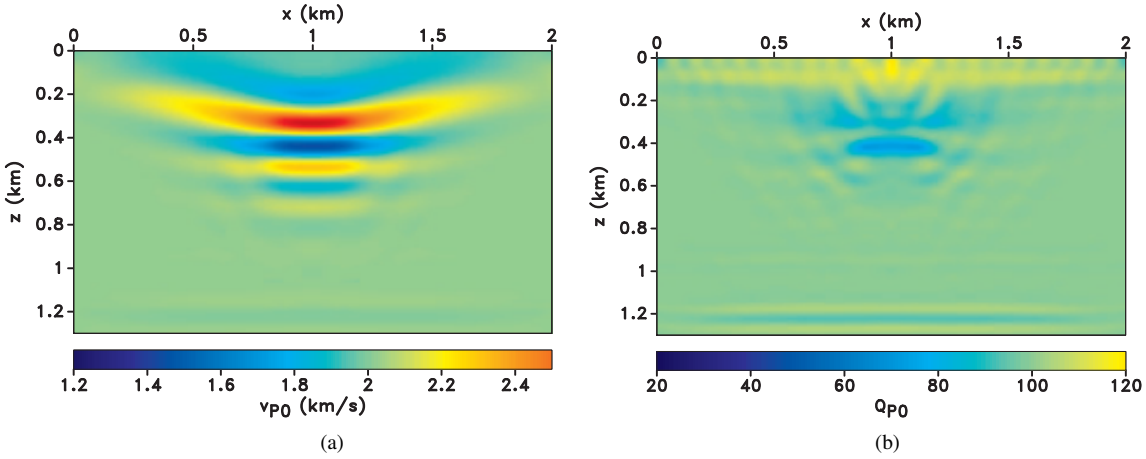

Figure 6. Recovered (a) v_{P0} and (b) Q_{P0} models obtained using the objective function $\mathcal{J}_D$. The inversion is not able to recover the low velocity anomalies and the deep reflector presented in the true models (Figure 1).

Figure 7 shows the recovered v_{P0} and Q_{P0} models when the objective function is defined with a petrophysical penalty based on multiple PDFs that exploit the spatial trends derived from the well logs (Figure 2). In this case, the reflector at $z = 1.25$ km (Figure 1) can be identified in both models as the petrophysical constraint $\mathcal{J}_P$ enforces that the properties of the models for the deep areas are different than the others (Figure 2), as one can notice by comparing Figure 3d to Figures 3a-c. Additionally, because of the PDF that describes the model for the region where the gas clouds are located (Figure 3b), the low velocity anomalies are recovered in both models (Figure 7). However, as the anomalies are thin and close to each other, and due to the relative small aperture and low frequency of 10 Hz used for inversion, FWI does not have sufficient resolution to separate the gas bodies. Notwithstanding, the inverted models depicted in Figure 7 are less affected by interparameter crosstalk effects than the models recovered using only the data misfit (Figure 6).

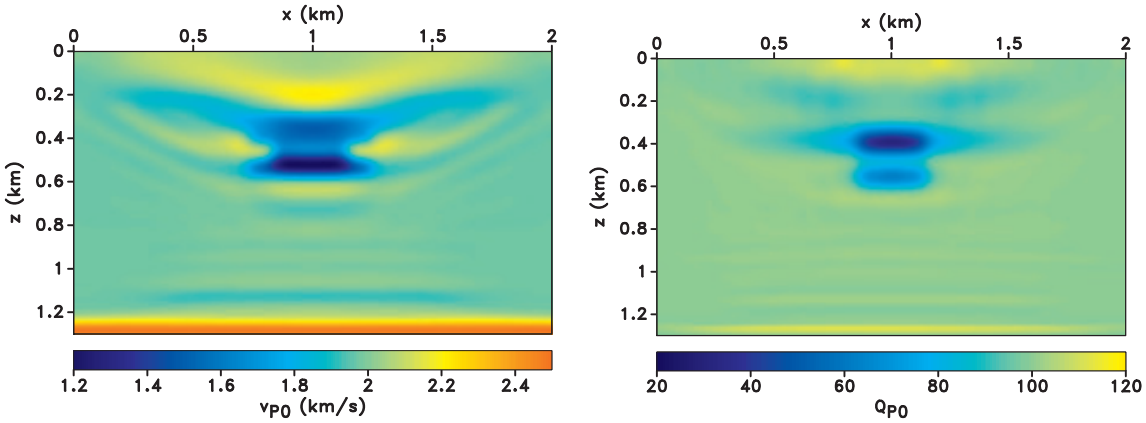

(a) (b)

Figure 7. Recovered (a) v_{P0} and (b) Q_{P0} models obtained using the objective function $\mathcal{J}_D + \mathcal{J}_P$, where $\mathcal{J}_P$ is based on multiple PDFs, which are determined considering spatial trends in the available petrophysical data (Figure 2).

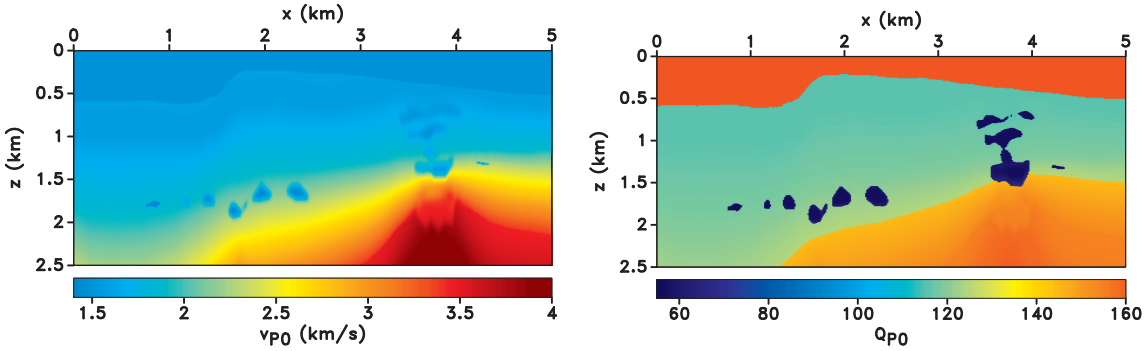

(a) (b)

Figure 8. BP 2004 Benchmark model: Synthetic models for the (a) v_{P0} and (b) Q_{P0}.

3.2 Model 2: BP 2004 Benchmark

The second synthetic example uses the right portion of the BP 2004 Benchmark model (Billette and Brandsberg-Dahl, 2005), which simulates a geological environment with localized slow velocity anomalies and shallow gas. The velocity estimation for this part of the BP model is considered very challenging due to the presence of the subtle velocity anomalies stacked on top of one-another. The original BP 2004 Benchmark model is acoustic and composed only of velocity and density models. Hence, in order to perform viscoelastic inversion, we use the original v_{P0} model (Figure 8a) to construct the attenuation parameters Q_{P0} (Figure 8b) and Q_{S0} (Figure 9b), as well as the shear velocity model v_{s0} (Figure 9a). We set 160 and 140 as the maximum values in the scale bar of all figures corresponding to Q_{P0} and Q_{S0}, respectively, for plotting purposes. For the water layer, we use $Q_{P0} = 10000$ and $Q_{S0} = 5000$, so A_{P0} and A_{S0} are approximately zero. We keep the velocity parameters v_{S0} (Figure 9a), ϵ and δ equal to their true values during the inversion. For this example, ϵ and δ are also constant and equal to 0.3 and 0.1, respectively. We also keep the attenuation parameter A_{S0} (Figure 9b) equal to its true values during the inversion, and set ϵ_Q and δ_Q equal to -0.05 and -0.1, respectively. We build the initial Q_{P0} (or A_{P0}) model by removing the gas and other low-velocity anomalies from the original model (Figure 8b) to investigate if we are able to recover these anomalies after the inversion.

We simulate a multicomponent ocean bottom seismic survey (OBS) with a line of receiver at the water bottom and 101 evenly spaced pressure sources located at $z = 0.02$ km. We use a 7.5 Hz peak Ricker source wavelet and initiate the inversion with the v_{P0} and Q_{P0} models depicted in Figure 10. We consider that prior petrophysical data from wells located at $x = 2.1$, 3.9 km are available. As in the previous example, we assume that an empirical A_{P0} well log derived from a given method is available, and we use the actual values extracted from the true model (Figure 8b) at the well locations. For this example, we set $c_1 = 1$ s/km and $c_2 = 400$.

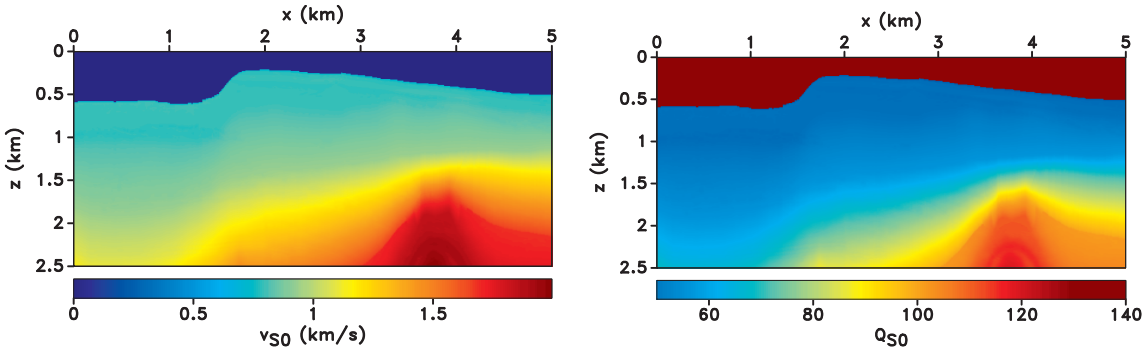

(a) (b)

Figure 9. BP 2004 Benchmark model: Synthetic models for the (a) v_{S0} and (b) Q_{S0}.

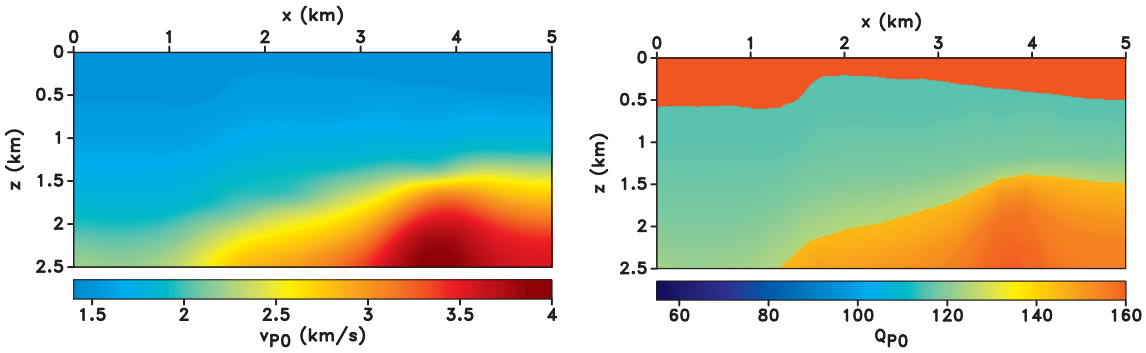

(a) (b)

Figure 10. BP 2004 Benchmark model: Initial models, (a) v_{P0} and (b) Q_{P0} used for the viscoelastic waveform inversion.

In order to define a penalty term based on multiple PDFs associated with spatial trends in the petrophysical data, we consider $K_i(\mathbf{m})$ operators for inversion that are not simply established using blocks defined from the depth extent of formations intercepted in the wells. We use the initial Q_{P0} model (Figure 10b) to define two zones of constant Q_{P0}, and define the mask operators depicted in Figure 11. We determine the probability distributions $f_1(\mathbf{p})$ and $f_2(\mathbf{p})$, using the well log data corresponding to each region (Figure 12). Figures 13a and 13b display the distances $D_1(\mathbf{m})$ and $D_2(\mathbf{m})$, and the correspondent gradient of the petrophysical terms for $f_1(\mathbf{p})$ and $f_2(\mathbf{p})$, respectively. As in the previous example, the distance $D_i(\mathbf{m})$ and the associated objective function-gradient are both zero when the model $\mathbf{m}$ at a given location in the updated model is consistent with the distribution given by its correspondent PDF.

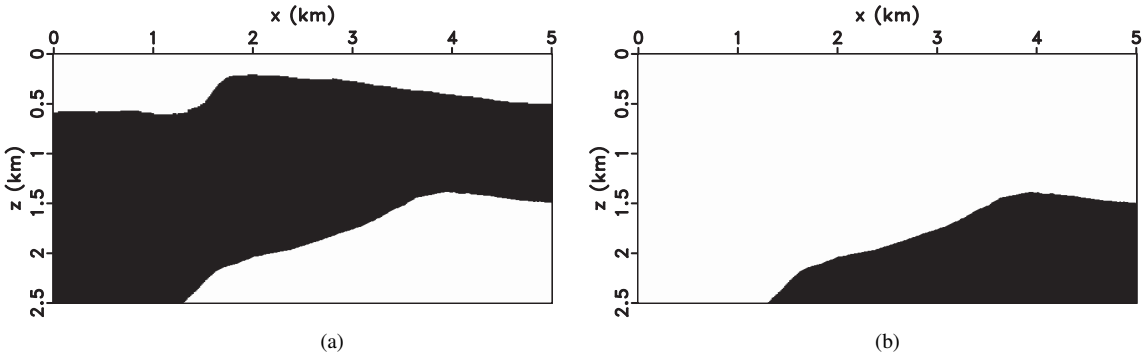

(a) (b)

Figure 11. BP 2004 Benchmark model: Mask operators (a) K_1 and (b) K_2 used to constrain PDFs at various corresponding spatial locations. Black regions corresponds to 1, and white to 0.

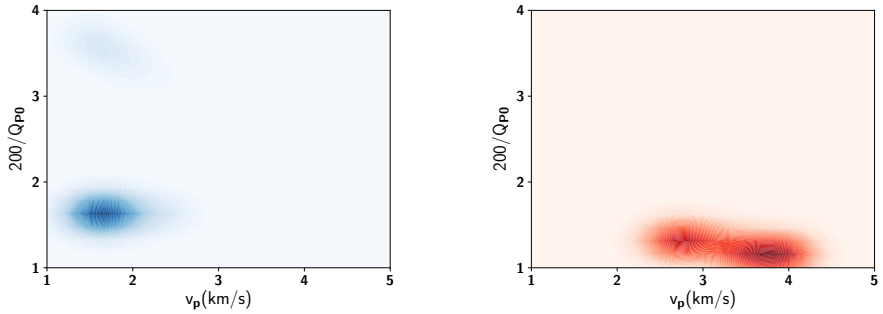

Figure 12. BP 2004 Benchmark model: The distributions (a) f_1 and (b) f_2 using the spatial trends in petrophysical information from the well log at $x = 2.1$ km and $x = 3.9$ km.

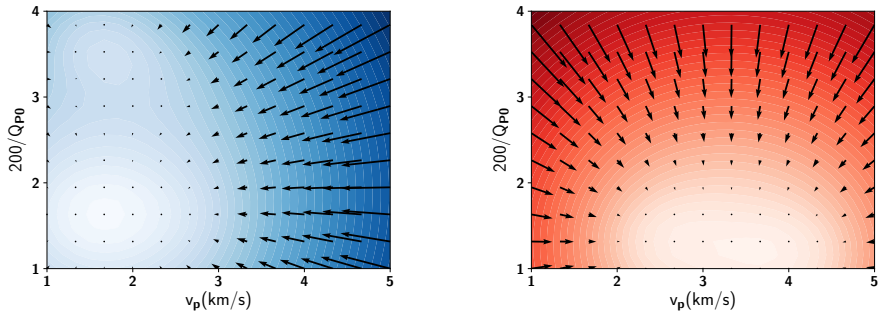

Figure 13. BP 2004 Benchmark model: The distances (a) $D_1(\mathbf{m})$ and (b) $D_2(\mathbf{m})$, and their gradients. As expected, the high probability models are associated with small values of $D_i(\mathbf{m})$ and with zero gradients.

Figure 14 shows the recovered v_{P0} and Q_{P0} models using the objective function $\mathcal{J}_D$. As we do not include petrophysical information during inversion, the gas clouds and other shallow anomalies are not well recovered during the inversion in both models. Additionally, without petrophysical information, the velocity errors cause higher errors in the attenuation model. As a consequence, both models are contaminated with non-geological artifacts due to parameter crosstalk, which severely deteriorates the quality of the recovered models.

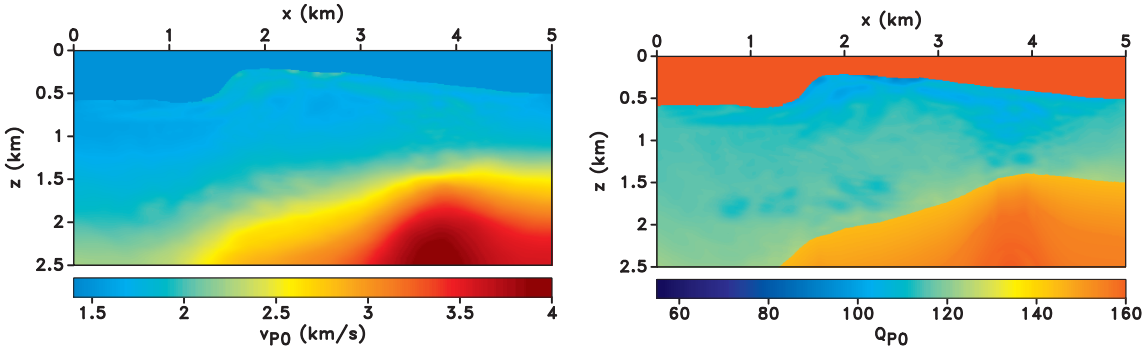

Figure 14. BP 2004 Benchmark model: Recovered (a) v_{P0} and (b) Q_{P0} models obtained using the objective function $\mathcal{J}_D$. The inversion is not able to recover the low velocity anomalies and the models are contaminated with high-wavenumber artifacts in addition to the artifacts due to the interparameter cross-talk between velocity and attenuation parameters.

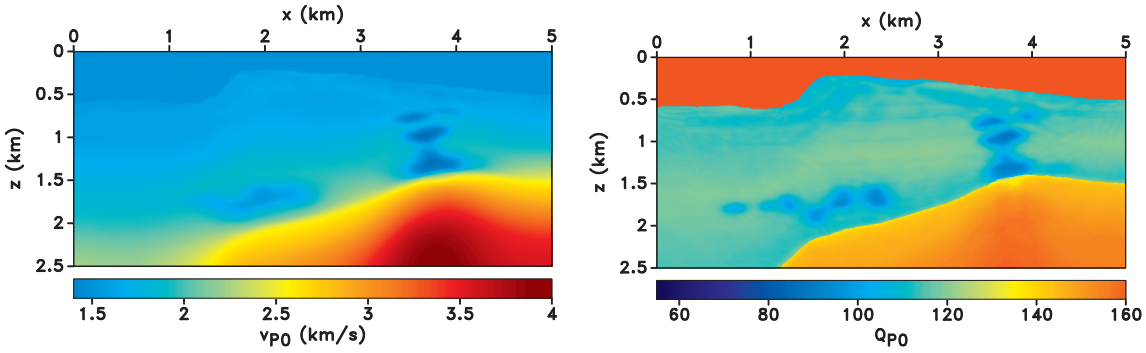

(a) (b)

Figure 15. BP 2004 Benchmark model: Recovered (a) v_{P0} and (b) Q_{P0} models obtained using the objective function $\mathcal{J}_D + \mathcal{J}_P$, where $\mathcal{J}_P$ is based on multiple PDFs, which are determined considering spatial trends in the available petrophysical data. With petrophysical penalties, the inversion is able to recover the low velocity anomalies in both models..

Figure 15 shows the recovered v_{P0} and Q_{P0} models when the objective function is based on multiple spatially-variable PDFs that use the mask operators shown in Figure 11. In this case, the gas anomalies and other shallow anomalies are well recovered (Figure 15). The recovered models depicted in Figure 15 are less affected by crosstalk artifacts and closer to true models (Figure 8) than the models inverted using only the data misfit (Figure 14). The recovered Q_{P0} shown in Figure 15b proves that the petrophysical penalty term based on multiple PDFs helps to recover the low velocity anomalies that are not present in the initial model (Figure 10b) when velocity and attenuation parameters are inverted simultaneously. In order to recover amplitudes for the low velocity anomalies that are closer to the true models (Figure 8), one can define a larger number of mask operators to delineate the spatial trends more accurately.

4 CONCLUSIONS

We describe an approach to incorporate petrophysical information into the objective function of viscoelastic full-waveform inversion using a penalty term based on multiple probability density functions that take into account the spatial distribution of petrophysical properties. By using this framework, we mitigate the artifacts created by the crosstalk between the velocity and attenuation parameters, while ensuring that the inversion delivers feasible subsurface models, and recover structures such as shallow low-velocity anomalies and deep reflectors that are not recovered when inversion is performed using only the data misfit. Our proposed method is directly applicable to monitoring carbon dioxide geological sequestration, as well as to monitoring production of multi-layer reservoirs.

5 ACKNOWLEDGMENTS

We acknowledge CAPES (Brazilian Federal Agency for Support and Evaluation of Graduate Education) for financial support. We thank the sponsors of the Center for Wave Phenomena (CWP), whose support made this research possible. The synthetic examples in this paper uses the Madagascar open-source software package (Fomel et al., 2013) freely available from http://www.ahay.org.

REFERENCES

Aragao, O., and P. Sava, 2020a, Elastic full-waveform inversion probabilistic petrophysical model constraints: Geophysics, **85**, no. 2, R101–R111.

———, 2020b, Elastic full waveform inversion with probabilistic petrophysical clustering: Geophysical Prospecting, **68**, no. 4, 1341–1355.

———, 2020c, Elastic full-waveform inversion with spatial probabilistic petrophysical constraints: SEG International Exposition and 90th Annual Meeting, Expanded Abstracts, 730–734.

Bai, J., D. Yingst, R. Bloor, and J. Leveille, 2014, Viscoacoustic waveform inversion of velocity structures in the time domain: Geophysics, **79**, no. 3, R103–R119.

Bai, T., and I. Tsvankin, 2016, Time-domain finite-difference modeling for attenuative anisotropic media: Geophysics, **81**, no. 2, C69–C77.

Bai, T., I. Tsvankin, and X. Wu, 2017, Waveform inversion for attenuation estimation in anisotropic media: Geophysics, **82**, no. 4, WA83–WA93.

Billette, F., and S. Brandsberg-Dahl, 2005, The 2004 BP velocity benchmark., *in* 67th Annual Internat. Mtg., EAGE, Expanded Abstracts: EAGE, B035.

Cheng, C. H., M. N. Toksoz, and M. E. Wills, 1982, Determination of in situ attenuation from full waveform acoustic logs: J. Geophys. Res., **87**, 5477–5484.

Fomel, S., P. Sava, I. Vlad, Y. Liu, and V. Bashkardin, 2013, Madagascar: open-source software project for multidimensional data analysis and reproducible computational experiments: Journal of Open Research Software, **1**.

Kamei, R., and R. Pratt, 2013, Inversion strategies for visco-acoustic waveform inversion: Geophysical Journal International, **194**, no. 2, 859–884.

Malinowski, M., S. Operto, and A. Ribodetti, 2011, High-resolution seismic attenuation imaging from wide-aperture onshore data by visco-acoustic frequency-domain full-waveform inversion: Geophysical Journal International, **186**, no. 3, 1179–1204.

Mavko, G., T. Mukerji, and J. Dvorkin, 2003, The rock physics handbook: tools for seismic analysis of porous media: Cambridge University Press.

Neep, J. P., 1995, Robust estimation of P-wave attenuation from full waveform array sonic data: J. Seis. Expl., **4**, 329–344.

Operto, J. S., P. Amestoy, J. Y. L'excellent, L. Giraud, and H. B. H. Ali, 2007, 3D finite-difference frequency-domain modeling of visco-acoustic wave propagation using a massively parallel direct solver: A feasibility study: Geophysics, **72**, no. 5, SM195–SM211.

Operto, J. S., A. Miniussi, R. Brossier, L. Combe, L. Metivier, V. Monteiller, A. ribodetti, and J. Virieux, 2015, Efficient 3-D frequency-domain mono-parameter full-waveform inversion of ocean-bottom cable data: Application for Valhall in the visco-acoustic vertical transverse isotropic approximation: Geophysical Journal International, **202**, 1362–1391.

Operto, S., Y. Gholami, V. Prieux, A. Ribodetti, R. Brossier, L. Metivier, and J. Virieux, 2013, A guided tour of multiparameter full-waveform inversion with multicomponent data: from theory to practice: The Leading Edge, **32**, no. 9, 1040–1054.

Ouellet, G. F., E. Gloaguen, and B. Giroux, 2017, Time domain viscoelastic full waveform inversion: Geophysical Journal International, **209**, 1718—-1734.

Plessix, R. E., 2006, A review of the adjoint-state method for computing the gradient of a functional with geophysical applications: Geophysical Journal International, **167**, no. 2, 495–503.

Plessix, R. E., A. Stopin, H. Kuehl, V. Goh, and K. Overgaag, 2016, Visco-acoustic Full Waveform Inversion: 78th European Association of Geoscientists and Engineers Conference and Exhibition, EAGE, Expanded Abstracts, 1–5.

Sun, X., X. Tang, C. H. Cheng, and L. N. Frazer, 2000, P- and S-wave attenuation logs from monopole sonic data: Geophysics, **65**, no. 2, 755–765.

Tarantola, A., 1984, Inversion of seismic reflection data in the acoustic approximation: Geophysics, **49**, 1259–1266.

Trinh, P. T., R. Brossier, L. Metivier, L. Tavard, and J. Virieus, 2019, Efficient time-domain 3D elastic and viscoelastic full-waveform inversion using a spectral element method on flexible Cartesian-based mesh: Geophysics, **84**, no. 1, P61–P83.

Virieux, J., and S. Operto, 2009, An overview of full-waveform inversion in exploration geophysics: Geophysics, **74**, no. 6, WCC1–WCC26.

Zhu, T., J. M. Carcione, and J. M. Harris, 2013, Approximating constant-Q seismic propagation in the time domain: Geophysical Prospecting, **61**, 931–940.